JOURNAL OF MATERIALS SCIENCE 37 (2002) 2949–2963

Crack growth in lamellar titanium aluminides containing beta phase precipitates

M. GRUJICIC*, G. CAO
Department of Mechanical Engineering, Program in Materials Science and Engineering, Clemson University, Clemson SC 29634, USA
E-mail: mica@ces.clemson.edu

Mode-I fracture behavior of fully-lamellar polycrystalline γ-TiAl + α_2-Ti_3Al intermetallic alloys and the role of Ti-V base β-phase precipitates of different thermodynamic stability have been studied using a finite element method. A rate-dependent, finite-strain, crystal-plasticity based materials constitutive model is used to represent the deformation behavior of both the γ-TiAl + α_2-Ti_3Al lamellar matrix and the β-phase precipitates. Within the matrix colonies, fracture is assumed to take place throughout the α_2-Ti_3Al lamellae. In addition, fracture along colony boundaries and matrix/precipitate interfaces is considered. The constitutive behavior of all fracture interfaces is modeled using a cohesive-zone formulation. The analysis is carried out using the commercial finite element program Abaqus/Standard within which the material state is integrated using an Euler-backward implicit formulation. The results obtained show that the main mechanism of crack growth is nucleation of secondary cracks along α_2-Ti_3Al lamellae ahead of the main crack and their subsequent link-up with the tip of the main crack. The resulting fracture resistance curve acquires the characteristic step-wise shape. Both stable and metastable β-phase precipitates are found to have a beneficial effect on the fracture resistance of the material. However, the effect is not very significant and metastable β-phase precipitates appear to be a little bit more beneficial. All these findings are consistent with their experimental counterparts.

1. Introduction

Titanium aluminides, due to their low density, high oxidation resistance and excellent retention of strength at high temperatures, are being currently considered as replacement materials for nickel-based superalloys in some sections of advanced jet engines. Consequently, over the last two decades a large variety of titanium aluminide microstructures have been developed. The most promising microstructures developed are generally referred to as *fully-lamellar, nearly-lamellar* and *duplex*. The fully lamellar microstructure consists of colonies (or grains) containing aligned platelets (lamellae) of γ-TiAl and α_2-Ti_3Al intermetallic phases [1]. In the case of the nearly-lamellar microstructure, the boundaries of γ-TiAl + α_2-Ti_3Al colonies and, in particular, three-colony junctions are decorated with fine γ-TiAl grains [1]. The duplex microstructure consists of a mixture of equiaxed γ-TiAl grains and γ-TiAl + α_2-Ti_3Al colonies [1]. The mechanical properties, in particular fracture toughness and tensile ductility, are greatly affected by the microstructure of TiAl-based materials. For example, at comparable levels of the tensile strength, fully lamellar material generally possesses higher fracture toughness, but lower tensile ductility in comparison to the nearly-lamellar or duplex materials. In the present work only the fully-lamellar titanium aluminides are considered. However, these materials are allowed to contain fine-scale ($\sim$10 μm) dispersions of the β-Ti-V based phase of various thermodynamic stability with respect to the orthotropic α''-martensite. As demonstrated by Grujicic and Dang [2], such β-phase dispersions can give rise to significant improvements in materials fracture toughness and tensile ductility.

The microstructure of individual γ-TiAl + α_2-Ti_3Al colonies consists of parallel γ-TiAl and α_2-Ti_3Al lamellae with the lamellar orientation varying from colony to colony. The α_2-Ti_3Al phase is generally the minor phase whose volume fraction is typically less than 20 vol%. The lamellae of the two phases generally do not alternate. Rather, several lamellae of the crystallographically-related variants of the γ-TiAl phase separate the adjacent α_2-Ti_3Al lamellae. The β-phase particles are, in general, preferentially located at three-colony junctions [2].

Experimental investigation of fracture in the fully-lamellar TiAl-based materials has been the subject of many studies over the last decade. These studies have yielded the following main observations: (a) fracture toughness is affected by the lamellar spacing and the colony size [1, 3, 4]; (b) fracture toughness of fully-lamellar materials in the single-crystalline form

*Author to whom all correspondence should be addressed.

(polysynthetically-twinned single crystals) is highly anisotropic and is controlled by the lamellar orientation [5]; (c) a number of toughening mechanism can be operational [2, 6]; (d) ternary and quaternary alloy additions can considerably enhance the fracture toughness [7]; (e) fracture occurs either within the α_2-Ti_3Al lamellae [8] or along α_2/γ lamellar interfaces and colony boundaries [1, 4, 9].

Over the last decade, extensive computer modeling and simulations of deformation and fracture phenomena in the TiAl-based materials have also been conducted. Only the studies most closely related to the subject of the present work are reviewed here. A detailed two-dimensional crystal plasticity analysis of deformation of polycrystalline γ-TiAl + α_2-Ti_3Al materials is carried out by Kad *et al*. [10, 11]. This analysis was subsequently extended by our group to include fracture along colony boundaries [12, 13], the three-dimensional effects [14, 15] and the effect of martensitic transformation in a secondary-phase dispersion [16, 17]. In these studies no explicit account of the lamellar microstructure is made. Rather a homogenization procedure is used to determine the effective properties of the γ-TiAl + α_2-Ti_3Al lamellar microstructure. Recently Arata *et al*. [18–20] conducted an in-depth finite element analysis of fracture initiation and crack propagation in multi-colony fully-lamellar materials with different lamellar orientations. In their analysis, Arata *et al*. [18–20], used a cohesive-zone framework [21, 22] to induce preferential fracture through the α_2-Ti_3Al phase while the deformation behavior of γ-TiAl + α_2-Ti_3Al lamellae is modeled using either a linear isotropic or a viscoplastic constitutive model. The study reveals the complex and interactive roles materials properties (e.g., strength and fracture toughness) and the presence of tough inter-colony boundaries play in controlling crack nucleation, crack-path selection as well as the dominant toughness mechanisms. The role of anti-plane shear (Mode III) on fracture behavior of lamellar γ-TiAl has been analyzed in two recent studies [23, 24].

In the present paper, the (normal Mode I) fracture analysis of Arata *et al*. [18–20] is extended to include the effect of stable and metastable β-phase discrete particles located along the colony boundaries and three-colony junctions. In addition, deformation behavior of the γ-TiAl + α_2-Ti_3Al lamellae is modeled using the crystal-plasticity model of Grujicic and Batchu [14] which incorporates the effect of plastic anisotropy, the phenomenon which must be considered in order to model incompatibilities in plastic flow between the adjacent lamellar colonies.

The organization of the paper is as follows: A simplified geometric model used to represent the microstructure of the fully lamellar material containing β-phase dispersions is discussed in Section 2.1. A brief overview of the constitutive law for the γ-TiAl + α_2-Ti_3Al lamellae is given in Section 2.2. The finite element procedure used is discussed in Section 2.3. The main results obtained in the present work are presented and discussed in Section 3. The key conclusions resulted from the present study are summarized in Section 4.

2. Computational model

2.1. Microstructural model

A schematic of the local microstructure consisting of three neighboring γ-TiAl + α_2-Ti_3Al lamellar colonies and a β-phase particle located at the three-colony junction is shown Fig. 1a. This microstructure is further simplified in the present work as shown in Fig. 1b. Lamellar colonies are assumed to have a regular hexagonal shape and to be all of the same size (diameter = 200 μm). Dispersed β-phase particles are assumed to be located only at the three-colony junctions, to be of hexagonal shape and to have same size (diameter = 100 μm). Transcolony fracture is assumed to occur within the α_2-Ti_3Al lamellae and since α_2-Ti_3Al lamellae are very thin (typically $\sim$1 μm), they are not considered explicitly. Rather, they are replaced with planar cohesive surfaces and their contribution to deformation is accounted for by properly modifying the constitutive relations for the γ-TiAl phase. Thus, the microstructure

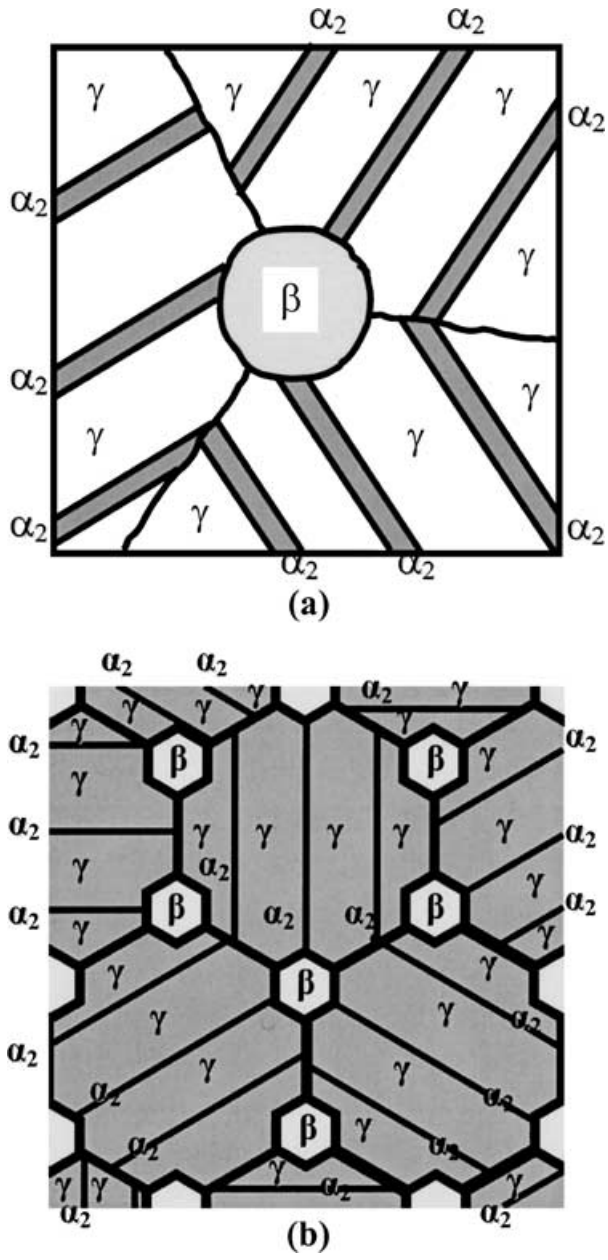

Figure 1 (a) A schematic of the microstructure near a three-colony junction in a γ-TiAl + α_2-Ti_3Al material containing dispersion of β-phase particles and (b) the microstructural model used in the present work.

of each colony is represented as a sequence of planar surfaces (represent the α_2-Ti_3Al lamellae) which divide the colony in a number of (α_2-modified) γ-TiAl platelets. The multivariant nature of the γ-TiAl lamellae between the adjacent α_2-Ti_3Al surfaces is not considered. Instead, they are considered as one continuous phase. To incorporate the effect of microstructural variability, the α_2-planar boundary of the adjacent colonies are assigned different orientations and their spacing and position are set at random. Thus, α_2-planar boundaries in one colony are not, in general, connected with the ones in the adjacent colony.

To mimic the overall brittleness of the lamellar structure, cohesive surfaces are placed along all colony boundaries and matrix/precipitate interfaces. To promote fracture along the α_2-phases, low values are assigned to their cohesive strength and the work of separation. In accordance with our experimental observations [2], considerably higher values of the cohesive strength and the work of separation are assigned to the matrix/precipitate interfaces. This substantially lowered the probability for fracture throughout these interfaces. The lamellar-colony boundaries are assigned intermediate fracture properties and, hence, they are made a potential crack path in addition to the α_2-lamellae.

In summary, the microstructural model used in the present work, Fig. 1b, has the following defining features:

(a) It is two dimensional in nature and, hence, can not account for out-of-plane lamellae misorientations which may play an important role in deformation and fracture;

(b) It approximates the shape of the lamellar colonies and dispersion particles as perfect hexagons and assumed that all colonies and all dispersion particles are of the same size;

(c) It neglects the finite width of the α_2-lamellae; and

(d) It neglects the multi-variant nature of the γ-TiAl lamellar structure between the adjacent α_2-lamellae.

2.2. Materials constitutive relations

2.2.1. Cohesive surfaces

The constitutive behavior of the cohesive surfaces is represented by the following traction (T) verses displacement (Δ) law which was originally proposed by Xu and Needleman [22]:

$$T_n = -\frac{\phi_n}{\delta_n}\exp\left(-\frac{\Delta_n}{\delta_n}\right)\left\{\frac{\Delta_n}{\delta_n}\exp\left(-\frac{\Delta_t^2}{\delta_t^2}\right) + \frac{1-q}{r-1}\left[r-\frac{\Delta_n}{\delta_n}\right]\times\left[1-\exp\left(-\frac{\Delta_t^2}{\delta_t^2}\right)\right]\right\} \quad (1)$$

$$T_t = -\frac{\phi_n}{\delta_n}\left(2\frac{\delta_n}{\delta_t}\right)\frac{\Delta_t}{\delta_t}\left\{q+\left(\frac{r-q}{r-1}\right)\frac{\Delta_n}{\delta_n}\right\} \times \exp\left(-\frac{\Delta_n}{\delta_n}\right)\exp\left(-\frac{\Delta_t^2}{\delta_t^2}\right) \quad (2)$$

$$q = \frac{\phi_t}{\phi_n}, r = \frac{\Delta_n^*}{\delta_n} \quad (3)$$

where the subscripts n and t denote normal and tangential surface separations, σ_{max} and τ_{max} represent respective maximum sustainable normal and shear tractions occurring at characteristic surface separations, δ_n and δ_t, and ϕ_n and ϕ_t are the corresponding works of complete separation under pure normal and pure shear conditions. Δ_n^* (set to zero in the present work) represents the value of Δ_n after complete shear separation under $T_n = 0$.

The normal and tangential displacements, Δ_n and Δ_t, are defined as $\Delta_n = n \cdot \Delta$ and $\Delta_t = t \cdot \Delta$ where n and t represent respectively unit vectors normal and tangential to the respective cohesive-surface segment in the current configuration; Δ represent the surface separation vector associated with the same surface segment and the raised dot denotes the scalar product.

For a given pure normal or shear mode of surface separation, σ_{max} (or τ_{max}), δ and ϕ are mutually related and hence only two out of three cohesive surface parameters (in each case) are independent and need to be specified. The work of separation governs the macroscopic fracture toughness of the materials and hence, ϕ_n and ϕ_t can be assessed using experimentally determined mode I and mode II critical stress intensely factors, K_{Ic} and K_{IIc}. However, separate ϕ_n and ϕ_t values are needed for α_2-Ti_3Al lamellae, γ-TiAl + α_2-Ti_3Al colony boundaries and matrix/precipitate interfaces for which the corresponding K_{Ic} and K_{IIc} data are presently not available. As far as the cohesive strengths, σ_{max} and $\tau_{max,}$ and the characteristic surface separations, δ_n and δ_t, are concerned, they can be determined using various theoretical approaches such as atomic-scale simulations [e.g., 12]. However, since continuum plasticity (including the local crystal plasticity model used in the present work) limits the maximum attainable stress levels at the crack tip, values for σ_{max} and τ_{max} (in the range of the materials strength) lower than their theoretical counterparts are used in the present work. Such values are found to give reasonable prediction for fracture behavior in structural metals [25]. Furthermore, since the mesh size needed to resolve the crack-tip fields scale with the characteristic surface separations, computational tractability demanded the use of δ_n and δ_t values considerably larger than their atomistic-simulation counterparts.

The cohesive-surface parameters for the α_2-planar surfaces, γ-TiAl matrix/β-Ti-V precipitate interfaces and γ-TiAl + α_2-Ti_3Al colony boundaries as proposed by Arata *et al.* [18–20] are summarized in Table I. It should be noted that for all surfaces it is assumed that $\phi_n = \phi_t$ and $\delta_n = \delta_t$. A parametric study of the effect of magnitudes of the cohesive surface parameters is not carried out in the present work.

2.2.2. Continuum phases

The constitutive responses of the γ-TiAl + α_2-Ti_3Al lamellar matrix and of the β-phase precipitates are represented using the crystal-plasticity models recently proposed by Grujicic and Zhang [12, 13] and Grujicic and Batchu [14]. Only the model of Grujicic and Batchu [14] for (polysynthetically-twinned) γ-TiAl + α_2-Ti_3Al single crystals will be reviewed here since

TABLE I Cohesive-surface parameters for α_2-Ti_3Al planar interfaces, γ-TiAl + α_2-Ti_3Al colony boundaries and γ-TiAl/β-Ti-V interfaces

		Interface/Boundary		
Parameter	Units	α_2-Ti_3Al	Lamellar-colony boundaries	γ-TiAl/β-Ti-V interfaces
Work of separation $\phi_n = \phi_t$	(J/m^2)	407.75	6,524.00	6,524.00
Normal strength σ_{max}	(GPa)	1.00	2.50	4.06
Shear strength τ_{max}	(GPa)	2.33	9.32	9.32
Characteristic surface separation $\delta_n = \delta_t$	(μm)	0.150	0.375	0.600

it represents is a generalization of the model proposed by Grujicic and Zhang [12, 13]. The model of Grujicic and Batchu [14] can be characterized a rate-dependent, isothermal, elastic-viscoplastic, finite-strain, crystal-plasticity model. It incorporates the experimental observation [e.g., 12] that plastic deformation in polysynthetically-twinned γ-TiAl + α_2-Ti_3Al single crystals parallel to the γ-TiAl + α_2-Ti_3Al lamellar interfaces is substantially easier (the soft mode) than deformation normal to these interfaces (the hard mode). Grujicic and Batchu [14] postulated that the soft-mode plastic deformation behavior of polysynthetically-twinned γ-TiAl + α_2-Ti_3Al single crystals is controlled by the $\{111\}\ \langle 1\bar{1}0\rangle$ slip systems of γ-TiAl with the slip direction parallel with the lamellar interfaces, while the hard mode plastic deformation is taken to be controlled by the $\{11\bar{2}1\}\ \langle 11\bar{2}6\rangle$ slip of α_2-Ti_3Al. Within the model, each material point is assumed to contain a single material whose response is obtained by proper homogenization of the two constituent phases, γ-TiAl and α_2Ti_3Al. The (initial) reference configuration in this material is taken to consist of a mixture of two perfect stress-free crystal lattices and the embedded material. The position of each material point in the reference configuration is given by its position vector X. In the current configuration, each material point is described by its position vector, x, and hence, mapping of the reference configuration into the current configuration is described by the deformation gradient, $F = \partial x/\partial X$. In order to reach the current configuration, the reference configuration must be deformed both elastically and plastically and, hence, the total deformation gradient can be multiplicatively decomposed into its elastic, F^e, and plastic, F^p, parts as $F = F^e F^p$. In other words, the deformation of a (polysynthetically-twinned) single-crystal material point is considered to be the result of two independent atomic-scale processes: (i) an elastic distortion of the crystal lattice(s) corresponding to the stretching of atomic bonds and; (ii) a plastic deformation which is the result of crystallographic slip and which leaves the crystal lattice(s) undisturbed.

The constitutive model of Grujicic and Batchu [14] is based on the following governing variables: (i) The Cauchy stress, T; (ii) The deformation gradient, F; (iii) Crystal slip systems, labeled by integers α. Each slip system is defined by a unit slip-plane normal n_0^α, and a unit vector m_0^α aligned in the slip direction, both defined in the reference configuration; (iv) The plastic deformation gradient, F^p, with $\det(F^p) = 1$ (plastic deformation by slip does not give rise to a volume change) and; (v) The slip system deformation resistance $s^\alpha > 0$ which has the units of stress.

Based on the aforementioned multiplicative decomposition of the deformation gradient, the elastic deformation gradient F^e which describes the elastic distortions and rigid-body rotations of the crystal lattice, can be defined by:

$$F^e \equiv FF^{p-1}, \quad \det F^e > 0. \tag{4}$$

The plastic deformation gradient, F^p, on the other hand, accounts for the cumulative effect of shearing on all slip systems in the crystal.

Since elastic stretches in intermetallic materials such as γ-TiAl and α_3-Ti_3Al are generally small, the constitutive equation for stress under isothermal conditions can be defined by the linear relation:

$$T^* = C[E^e] \tag{5}$$

where C is a fourth-order elasticity tensor, and E^e and T^* are respectively the Green elastic strain measure and the second Piola-Kirchhoff stress measure relative to the isoclinic configuration obtained after plastic shearing of the lattices as described by F^p.

The evolution equation for the plastic deformation gradient is defined by the plastic velocity gradient, L^p, as:

$$L^p = \dot{F}^p F^{p-1} = \sum_\beta \dot{\gamma}^\alpha S_0^\alpha, \quad S_0^\alpha = m_0^\alpha \otimes n_0^\alpha, \tag{6}$$

where S_0^α is the Schmid tensor and $\otimes$ denotes the tensorial product of the vectors.

The plastic shearing rate $\dot{\gamma}^\alpha$ on a slip system α is described using the following simple power-law relation:

$$\dot{\gamma}^\alpha = \dot{\tilde{\gamma}} \frac{|\tau^\alpha|^{1/m}}{|S^\alpha|} \operatorname{sign}(\tau^\alpha) \tag{7}$$

where $\dot{\tilde{\gamma}}$ is a reference plastic shearing rate, τ^α and s^α are the resolved shear stress and the deformation resistance on slip system α, respectively and m is the material rate-sensitivity parameter.

Since elastic stretches in intermetallic materials are generally small, the resolved shear stress on slip system α can be defined as:

$$\tau^\alpha = T^* \cdot S_0^\alpha \tag{8}$$

where the raised dot denotes the scalar product between two second order tensors.

Finally, the slip system resistance is taken to evolve as:

$$\dot{S}^\alpha \sum_\beta h^{\alpha\beta} |\dot{\gamma}^\beta| \tag{9}$$

where $h^{\alpha\beta}$ describes the rate of strain hardening on the slip system α due to the shearing on the coplanar

(self-hardening) and non-coplanar (latent-hardening) slip systems β and is given the following simple form:

$$h^{\alpha\beta} = q^{\alpha\beta} h^{\beta} \tag{10}$$

where h^{β} denotes the self-hardening rate while $q^{\alpha\beta}$ is a matrix describing the latent hardening behavior for which the following simple form is adopted:

$$q^{\alpha\beta} = \begin{cases} 1 & \text{if } \alpha \text{ and } \beta \text{ are coplanar slip systems,} \\ q_1 & \text{otherwise} \end{cases} \tag{11}$$

The self-hardening rate h^{β} is defined as:

$$h^{\beta} = h_0^{\beta} \left| 1 - \frac{S^{\beta}}{S_s^{\beta}} \right|^{\tau} \operatorname{sign}\left(1 - \frac{S^{\beta}}{S_s^{\beta}} \right). \tag{12}$$

where h_0^{β} is the initial hardening rate and S_s^{β} the saturation slip deformation resistance and r a power exponent.

The finite element analysis of fracture in the material at hand requires integration of the state of γ-TiAl + α_2-Ti_3Al matrix and β-phase precipitate materials represented by Equations 4–12 along the loading path. An Euler-backward implicit formulation is used in the present work. A detailed description of this procedure and its implementation in a user material (UMAT) subroutine of the finite element package Abaqus/Standard [24] is given in our previous work [2].

2.3. Slip geometry

2.3.1. γ-TiAl + α_2-Ti_3Al lamellar phase

It is well-established experimentally [e.g., 1] that γ-TiAl and α_2-Ti_3Al lamellae have the following orientation relationship: $(0001)_{\alpha 2}//\{111\}_{\gamma}$ and $\langle 1120\rangle_{\alpha 2}//\langle 110\rangle_{\gamma}$ and that the lamellae interfaces are parallel to $(0001)_{\alpha 2}//\{111\}_{\gamma}$. To make the computations tractable, full three-dimensional crystal plasticity behavior of the γ-TiAl + α_2-Ti_3Al material (as well as that of the β-phase) is not carried out. Rather, following Kad *et al.* [10], a two-dimensional approximation is used within which the γ-TiAl + α_2-Ti_3Al material is projected onto a $(121)_{\gamma}//(1010)_{\alpha 2}$ plane. Within such two-dimensional model, in-plane slip is controlled by three slip systems: (a) The projected $\langle 110]\{111\}_{\gamma}$ slip system which controls the soft-mode slip, and (b) and (c) two projected $(1121)[1126]_{\alpha 2}$ pyramidal slip systems which control the hard-mode plastic deformation. As shown in Fig. 2a, the slip directions corresponding to these three slip systems designated as m_1, m_2, and m_3 form an isosceles triangle with an angle $\phi \sim 58^{\circ}$ between the soft and the hard slip systems. The crystal-plasticity materials constitutive parameters for the γ-TiAl + α_2-Ti_3Al lamellar-matrix phase used in the present work are the ones recently reported by Grujicic and Batchu [14] and, hence, are not presented here.

2.3.2. Stable β-Ti-V dispersed phase

The stable β-phase dispersed particles have the b.c.c. crystal structure in which slip occurs in four $\langle 111\rangle$ directions on {110}, {112} and {123} planes. The in-plane slip in this phase is simplified in the following way: The four $\langle 111\rangle$ directions are projected on an arbitrary plane associated with the [001] zone axis resulting in four slip systems m_1, m_2, m_3 and m_4 Fig. 2b. The Miller indices of this plane (730) are generated using a random number generator. The angles between these four slip systems given in Fig. 2b are kept fixed for all β-phase particles. However, the orientation of each particle is made different by selecting the Euler angle ψ at random. The crystal-plasticity parameters for the stable Ti-V-base β-phase have been recently reported by Grujicic and Sankaran [127] and, hence, are not given in the present paper.

2.3.3. Metastable β-Ti-V dispersed phase

The metastable β-phase undergoes a b.c.c. $\rightarrow$ h.c.p. martensitic transformation under stress. According to

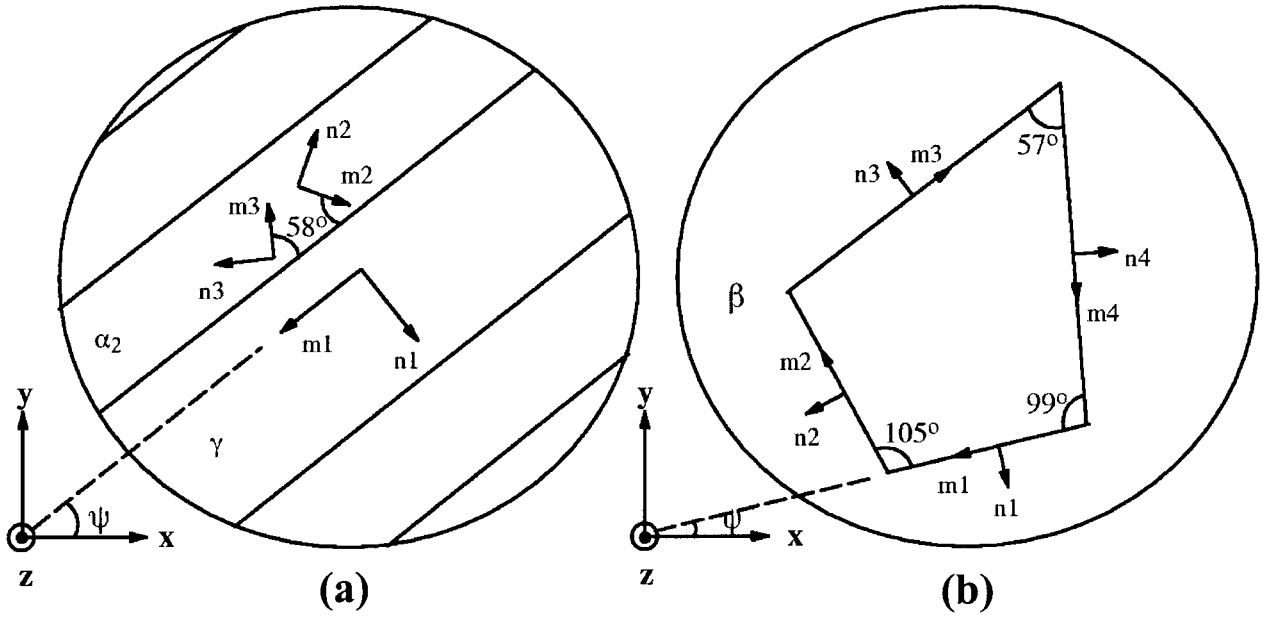

Figure 2 The projected slip systems used in the present finite element analysis of (a) the γ-TiAl + α_2-Ti_3Al matrix and (b) β-phase precipitates.

Burgers [28], the b.c.c. → h.c.p. martensitic transformation can be described in terms of two elemental processes: (a) shuffling of the parallel adjacent (110) planes in the opposite $[1\bar{1}0]$ direction and (b) pure shear on the $\{11\bar{2}\}$ planes in the $\langle 111\rangle$ directions. The shuffling produces the required h.c.p.-type ABAB stacking of the close packed $(0001)_{\text{h.c.p.}}$ planes and causes a volume change but does not give rise to shear. The transformation shear, on other hand, converts the irregular-hexagonal atomic arrangement in the $(110)_{\text{b.c.c.}}$ planes into the regular-hexagonal atomic arrangement in the close packed $(0001)_{\text{h.c.p.}}$ planes. Since for the b.c.c. → h.c.p. transformation to take place both shuffling and pure shear have to occur, and the shear directions $\langle 111\rangle$ are the same as those for slip, the b.c.c. h.c.p. transformation can be modeled as crystallographic slip which produces not only shear but also dilation [12, 13]. However, the fact that in metastable β-phase, crystallographic slip and the b.c.c. → h.c.p. martensitic transformation operate simulataneously as deformation mechanisms and that the relative contributions of the two to the overall plastic strain changes during loading, makes modeling of the constitutive response of the metastable β-phase quite challenging [12, 13]. In the present work, the approach of Grujicic and Zhang [12, 13] is utilized within which the effect of martensitic transformation is included through modification of the velocity gradient term, Equation 6. A modified velocity gradient term, $L^{\text{p}*}$, is introduced as:

$$L^{\text{p}*} = L^{\text{p}} = f(\varepsilon^{\text{p}})\left(\frac{2}{3}\text{sym}\, L^{\text{p}} \cdot \text{sym}\, L^{\text{p}}\right) I \qquad (13)$$

where L^{p} is given by Equation 6, I is the second order identity tensor and the function $f(\varepsilon^{\text{p}})$ incorporates the experimental observation [2] that the martensitic transformation in the metastable β-phase initially dominates plastic behavior, while at larger levels of the equivalent

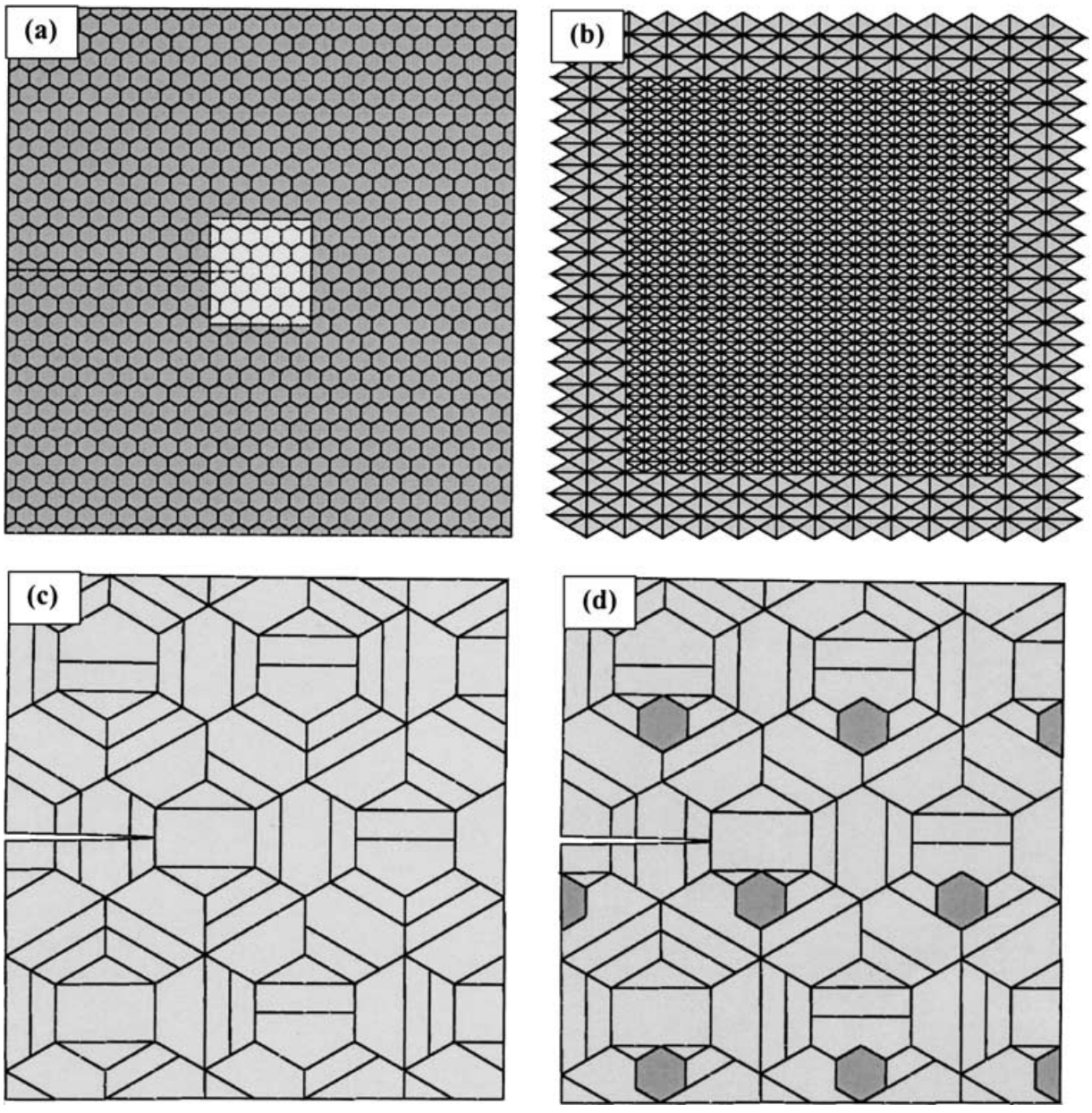

Figure 3 (a) Computational domain partitioned into hexagonal colonies; (b) Finite element discretization of the innermost region and the surrounding region of the computational domain; (c) cohesive-zone boundaries and interfaces used to study fracture in the material without β-phase precipitates; and (d) same as in (c) but in the material containing β-phase precipitates.

plastic strain, ε^{p}, the crystallographic slip becomes the dominant mode of deformation. The following $f(\varepsilon^{\mathrm{p}})$ function for the Ti-V β-phase, originally derived by Grujicic and Sankaran [25] is used in the present work:

$$f(\varepsilon^{\mathrm{p}}) = \begin{Bmatrix} 15.105(\varepsilon^{\mathrm{p}})^2 - 1.55\varepsilon^{\mathrm{p}} + 0.040 & \varepsilon^{\mathrm{p}} \angle 0.048 \\ 0 & \varepsilon^{\mathrm{p}} \geq 0.048 \end{Bmatrix} \tag{14}$$

In order to account for dynamic softening which dominates transformation in its early stages and static hardening which dominates transformation in its later stages, the self-hardening rate, Equation 12, is redefined as [12, 13]:

$$h^{\beta} = -16{,}180.349(\gamma^{\beta})^3 = 2{,}586.213(\gamma^{\beta})^2 - 89.884\gamma^{\beta} - 1.802 \times 10^9 \tag{15}$$

where γ^{β} is the accumulated shear strain associated with slip system β in the β-phase. The remaining crystal-plasticity parameters for the metastable β-phase are given in reference [27], It should be noted that Equation 15 reduces the overall hardening rate but does not generally cause the hardening rate to become negative and, hence, the field equations retain their ellipticity during simulations.

2.4. Multi-colony finite element method

2.4.1. Finite element meshes

Mode-I fracture in γ-TiAl + α_2-Ti_3Al fully lamellar structure without and with a dispersion of the β-phase precipitates is analyzed using a 4,330 μm × 4,500 μm computational domain. The domain is partitioned into hexagonal cells of equal size (200 μm), Fig. 3a. Each cell is set to represent a γ-TiAl + α_2-Ti_3Al lamellar colony. The computational domain is next divided into two regions: the innermost 866 μm × 900 μm region and the surrounding square-frame shaped region, Fig. 3a. Both of these regions are discretized using 3-node plane-strain elements (CPE3-Abaqus designation). The angles and edge sizes of the triangular elements are selected in such a way that 24 neighboring

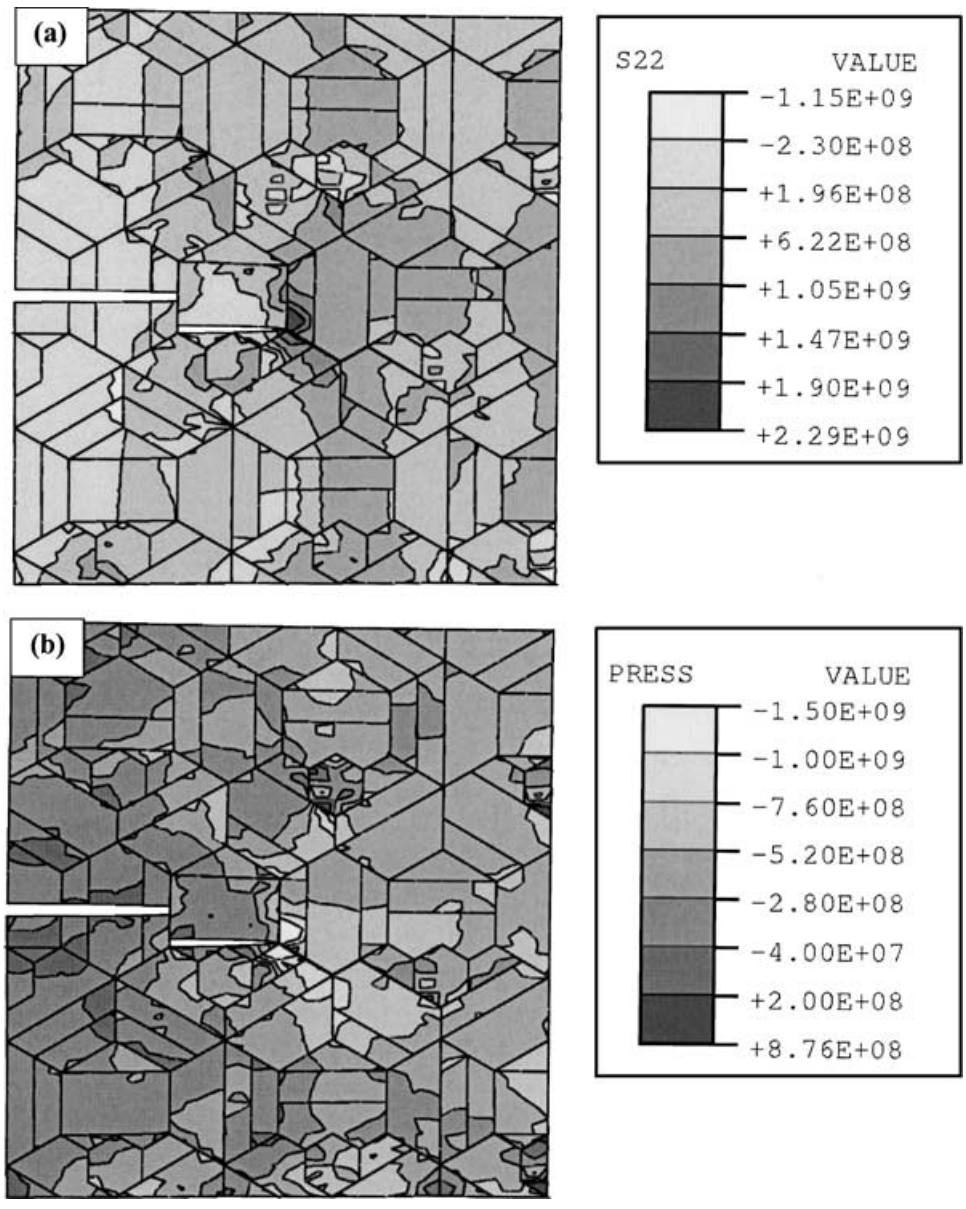

Figure 4 (a) Normal stress, σ_{22} (Pa); (b) pressure, $-\sigma_h$ (Pa); (c) equivalent plastic strain, $\bar{\varepsilon}^{\mathrm{pl}}$; and (d) total lattice rotation angle, $\Delta\psi$, contour plots in the γ-TiAl + α_2-Ti_3Al without β-phase precipitates at the stress intensity factor $K_1/K_{\mathrm{Ic0}}^{\alpha 2} = 4.0$. (*Continued*.)

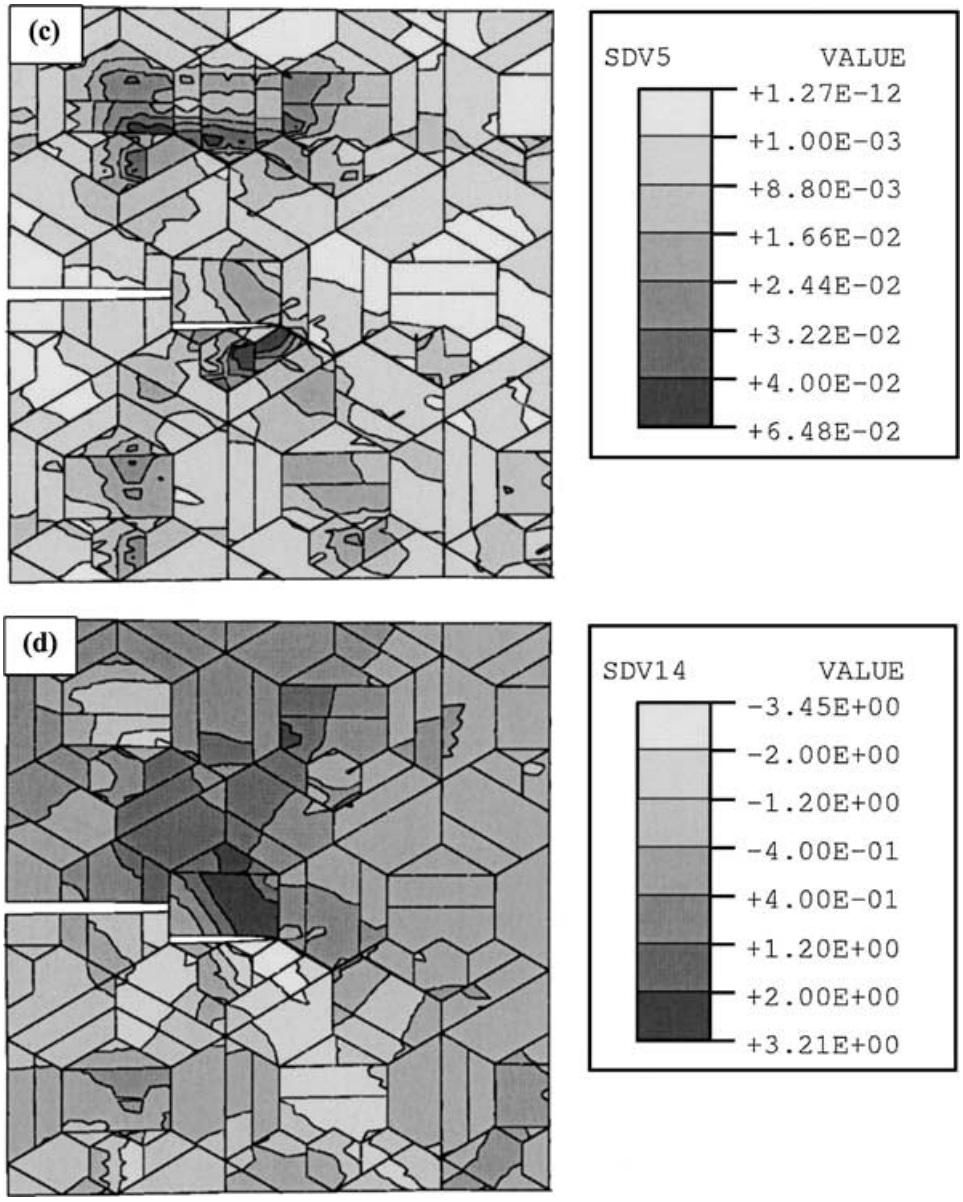

Figure 4 (*Continued*.)

elements form a perfect hexagon. The edge sizes of the elements in the inner region of the computational domain are set to be one half of the ones in the outer region, Fig. 3b. The inner region is divided into 2,880 CPE3 elements while the outer region into 17,280 CPE3 elements. Each hexagonal cell in the inner region is defined in terms of 96 elements, while a cell of the same size in the outer region is set to contain only 24 elements. Next, two α_2-Ti_3Al planes boundaries are assigned to each hexagonal cell within the inner region. The orientation of these boundaries is selected at random between the four possible orientations: 0°, 30°, 90° and 150°, relative to the horizontal x-axis. The spacing and the location of the two α_2Ti_3Al planar boundaries is also assign at random, Fig. 3c.

The same finite element mesh was used to study fracture in γ-TiAl + α_2-Ti_3Al containing β-phase particles. However, in addition to hexagonal cells used to represent the lamellar colonies discussed earlier, nine smaller (100 μm) hexagonal cells are defined in the inner computational region, Fig. 3d. The later cells are placed at the three-colony junctions formed by cells of the former type. CPE3 elements are used to define each β-phase hexagonal cell, giving rise to an effective volume fraction of the β-phase of 0.0625 within the inner computational region.

As discussed earlier, interfacial finite elements are placed along all fracture surfaces. The stiffness matrix of these elements is derived in terms of the corresponding cohesive-zone parameters and implemented in the user element (UEL) subroutine of Abaqus [26]. A detail account of this procedure is presented in our recent work [12].

2.4.2. Boundary conditions

The initial configuration of the computational crystal is assumed to be stress-free and not to contain any lattice perturbation. The multi-colony aggregates shown in Fig. 3c and d are assumed to contain a (fatigue-induced) crack. This crack is notated as the initial crack and its location is shown in Fig. 3c and d. In each case, the computational domain is loaded by prescribing the mode-I displacements along its outer boundary.

3. Results and discussion

3.1. Beta-phase free γ-TiAl + α_2-Ti_3Al material

In this section, the results of the finite element analysis of the mode I fracture behavior of the γ-TiAl + α_2-Ti_3Al material free of β-phase precipitates are presented and discussed.

The normal stress σ_{22}, the hydrostatic pressure $-\sigma_h$, the equivalent plastic strain ε^p and the total lattice rotation angle $\Delta\psi$ contour plots in the inner region of the computational domain at the normalized stress intensity factor $K_{Ic}/K_{Ic0}^{\alpha 2} = 4.0$ are shown in Fig. 4a–d, respectively. The critical stress intensity factor, $K_{Ic0}^{\alpha 2}$, used in the definition of the normalized stress intensity factor, $K_I/K_{Ic0}^{\alpha 2}$, is defined as:

$$K_{Ic0} = \sqrt{\frac{E^{\alpha_2}\phi_n^{\alpha_2}}{1-\nu^{\alpha_2}}} \tag{16}$$

and corresponds to the unstable crack growth along the α_2-Ti_3Al planar surfaces in the absence of plastic deformation.

Examination of Fig. 4a shows that the normal stress σ_{22} has the highest positive (tensile) values right in front of the crack tip. In fact, as expected, the entire region to the right of the crack tip experiences high tensile stresses. It should be noted that the initial crack has extended along the α_2-Ti_3Al planar interface in the γ-TiAl + α_2-Ti_3Al colony located to be right of the tip of initial crack. Further examination of Fig. 4a shows some relaxation of the normal stress in the wake of the crack.

The results shown in Fig. 4b indicate that the largest values of the negative pressure (tensile hydrostatic stress) are found in the region ahead of the crack tip. This high value of the tensile hydrostatic stress is responsible for the continuing crack advancement.

Examination of Fig. 4c reveals that the equivalent plastic strain is not only non-uniformly distributed at the length scale of the inner computational region but also within individual γ-TiAl + α_2-Ti_3Al colonies. This finding is fully consistent with the fact that the local extent of plastic deformation is controlled by the orientation of the slip systems (particularity the ones associated with the "soft" mode slip) relative to the applied stress field and by the constraints imposed by the surrounding colonies. The effect of constraints imposed by the surrounding colonies to be plastic deformation of a given colony can be further inferred from the total lattice rotation angle contour plot shown in Fig. 4d. The results shown in this figure show that in general the lattice rotation is non-uniform throughout the colony and that due to incompatibilities in plastic deformation and the resulting constraints imposed by the surrounding colonies on the plastic deformation of a given colony, the lattice rotation angles in the adjacent colonies are generally mutually comparable near three-colony junctions.

The crack extension and the selection of fracture path as a function of the increasing applied normalized stress intensity factor $K_{Ic}/K_{Ic0}^{\alpha 2}$ in the γ-TiAl + α_2-Ti_3Al material free of β-phase precipitates are shown in Fig. 5a–d. The corresponding fracture-resistance plot showing the extension of the main-crack tip, Δa, as a function of the applied normalized stress intensity factor, $K_{Ic}/K_{Ic0}^{\alpha 2}$, is shown in Fig. 6a. To improve clarity of Fig. 5a–d, a displacement magnification factor of 5 is used and only the portion of the inner computational

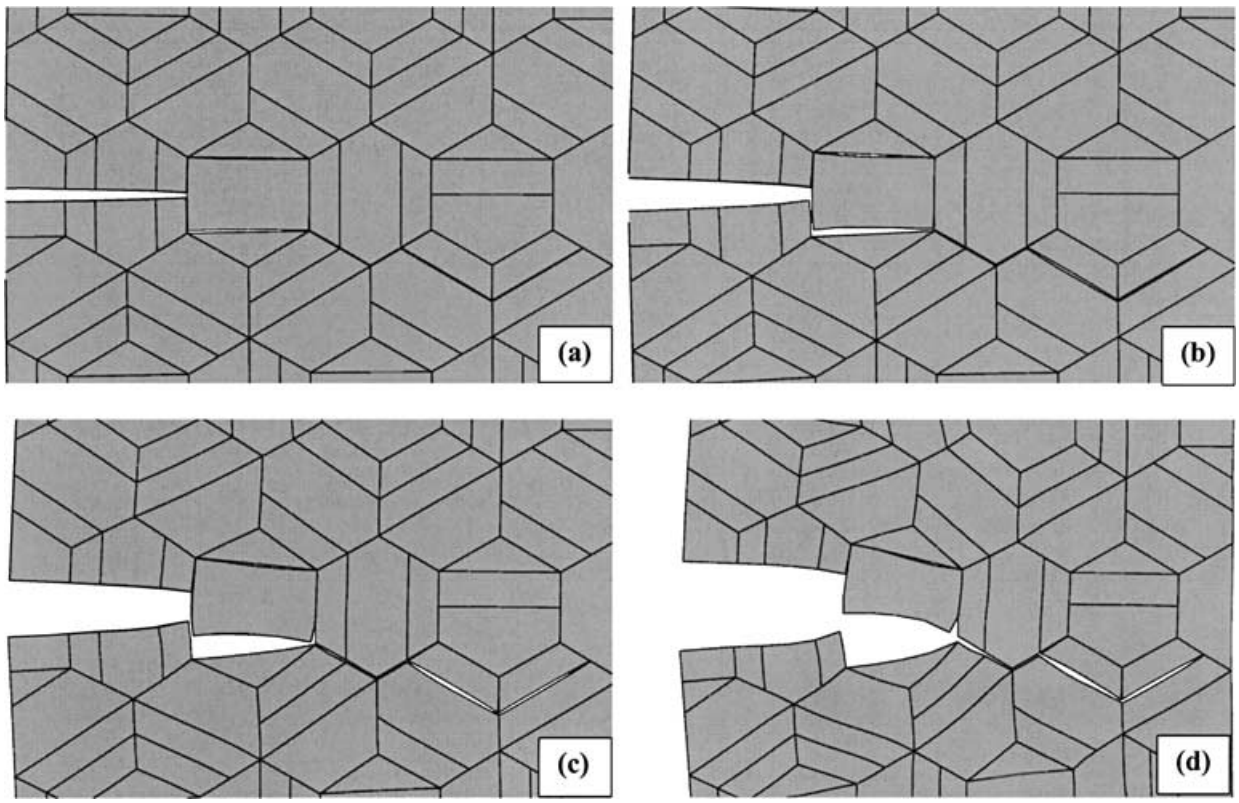

Figure 5 Crack trajectory at four levels of the normalized stress intensity factor $K_I/K_{Ic0}^{\alpha 2}$ of (a) 0.77; (b) 1.67; (c) 2.53; and (d) 4.00 in γ-TiAl + α_2-Ti_3Al without β-phase precipitates.

domain containing the crack trajectory is shown. Also, the colony boundaries and α_2-Ti_3Al lamellar surfaces are shown in order to help establish relationships between the materials microstructure and the crack path. The tip of the crack is arbitrarily defined as the location at the cohesive surface at which $\Delta_n = 2\delta_n$.

At the lowest level of the normalized stress intensity factor $K_{Ic}/K_{Ic0}^{\alpha 2} = 0.77$, Fig. 5a, the main crack has not advanced from its initial position. However, decohesion along the α_2-Ti_3Al planar surface in the γ-$TiAl + \alpha_2$-Ti_3Al colony just to the right of the crack tip of the initial crack is evident. Thus in addition to the main (initial) crack, the material contains at least one secondary crack. Since the fracture-resistance plot reflects the behavior of the main crack, the applied stress intensity factor increases while the extension of the tip of the main crack is minimal in this regime of material fracture, Fig. 6a.

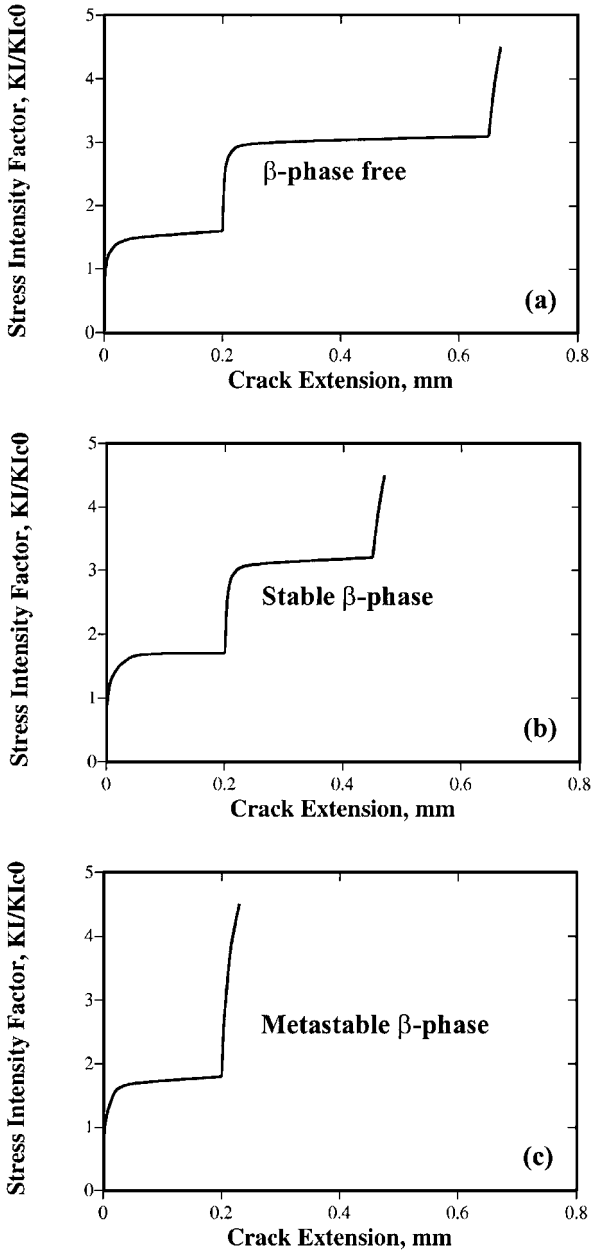

Figure 6 Variation of the crack tip advancement as a function of the applied normalized stress intensity factor in the γ-$TiAl + \alpha_2$-Ti_3Al without β-phase precipitates, (a), with stable β-phase precipitates, (b); and with metastable β-phase precipitates, (c).

As the applied stress intensity factor increases, the ligament which separates the tip of the main (initial) crack and the secondary crack in the γ-$TiAl + \alpha_2$-Ti_3Al colony just ahead of the tip of the main crack experiences an increasing loading. Consequently, at a sufficiently high level of the applied stress intensity factor, the ligament gives away and the main crack and the secondary crack connect. The resulting crack morphology is shown in Fig. 5b. In addition, at the instant when the two cracks connect, the main crack experiences an abrupt increase in its length at an effectively constant level of the applied stress intensity factor, Fig. 6b.

As the applied loading is further increased, no noticeable extension of the tip of the main crack takes place. Some decohesion along the colony boundaries just ahead of the main-crack tip takes place. However, this decohesion is still in the stable region (i.e., $\Delta_n < \delta_n$) and hence, does not result in crack-tip extension. In addition, considerable decohesion takes place along two α_2-Ti_3Al planar surfaces in two γ-$TiAl + \alpha_2$-Ti_3Al colonies to the right and somewhat lower relative to be branched main crack. In this region of crack growth, the applied normalized stress intensity factors, $K_{Ic}/K_{Ic0}^{\alpha 2}$, increases while the resulting crack-tip extension is minimal, Fig. 6a.

As the applied normalized stress intensity factor $K_{Ic}/K_{Ic0}^{\alpha 2}$ is further increased, the colony-boundary ligament separating the main-crack tip and the secondary cracks ahead of it, undergoes a complete decohesion giving rise to a link up between the main crack and the secondary cracks, Fig. 5d. Consequently, the crack tip undergoes a significant advancement at an essentially constant level of the applied stress intensity factor, Fig. 6a.

These observations are quite consistent with their experimental counterparts in a fully-lamellar Ti-46.6 at.% Al alloy recently reported by Chan *et al.* [7], Chan *et al.* [7] carried out fracture toughness measurements on compact tension specimens in an scanning election microscope (SEM) equipped with a loading stage. Both the fracture resistance (the stress intensity factor, K_I, versus the crack extension, Δa) curves and the crack trajectories were determined. The determination of the latter was carried out by directly observing one of the (previously polished and etched) side surfaces of a fatigue-pre-cracked compact tension specimens. This enabled establishment of correlations between the crack path and the attending materials microstructure. The main observations made by Chan *et al.* [27] can be summarized as followings:

(a) Crack advance within the lamellar colonies proceeds exclusively along the α_2-Ti_3Al lamellae with very little evidence of plastic deformation at the crack tip;

(b) The predominant mechanism of crack advancement at a length scale larger than the average lamellar-colony size appears to be nucleation of micro-cracks ahead of the main crack and the subsequent linking up of the micro-cracks and the main crack.

(c) When a crack traverses the colony and reaches a colony boundary, its ability to advance into the

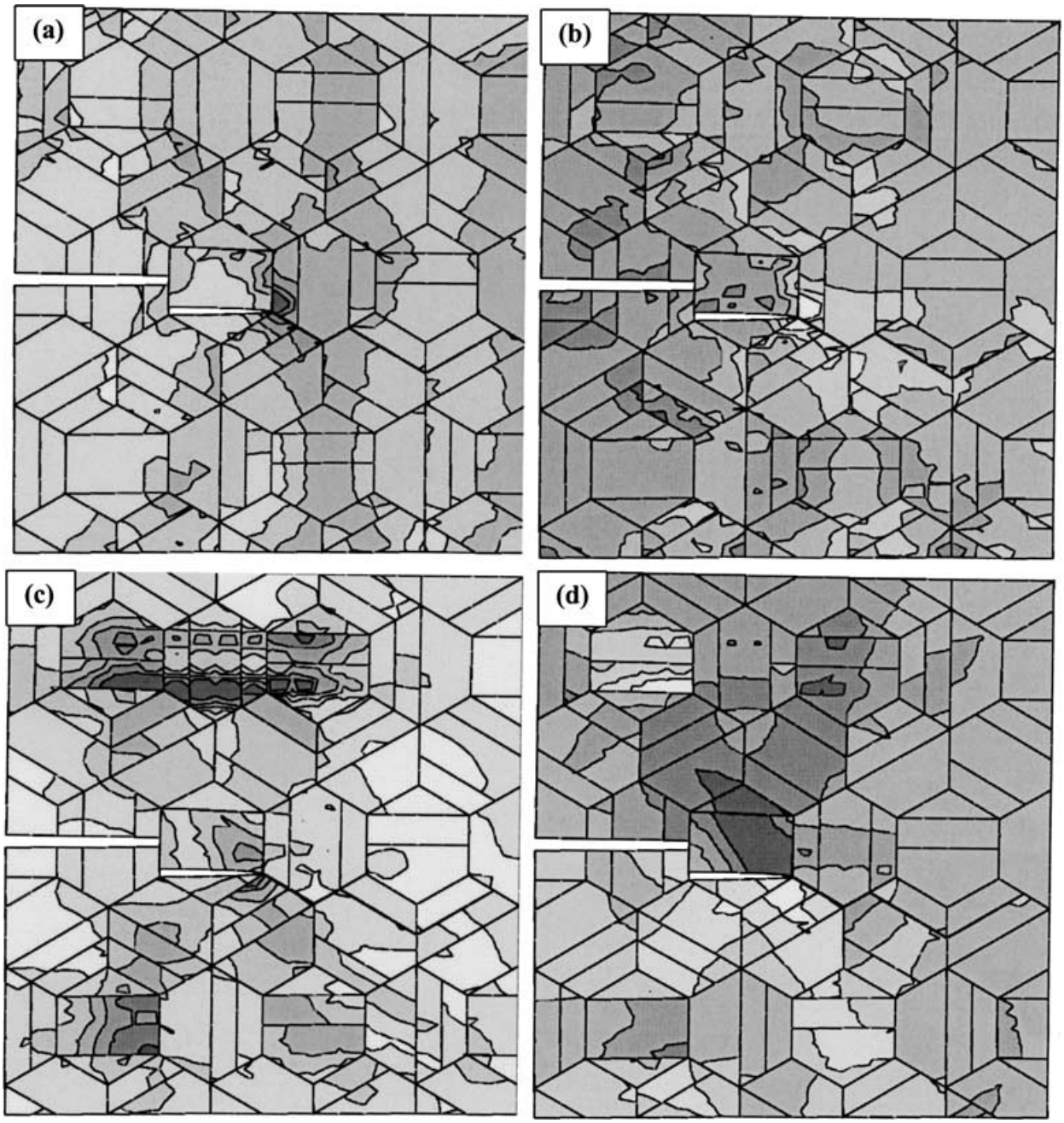

Figure 7 (a) Normal stress, σ_{22}; (b) pressure, $-\sigma_h$; (c) equivalent plastic strain, $\bar{\varepsilon}^{pl}$; and (d) total lattice rotation angle, $\Delta\psi$, contour plots in the γ-TiAl + α_2-Ti_3Al containing stable β-phase precipitates at the stress intensity factor $K_I/K_{Ic0}^{\alpha 2} = 4.0$. See Fig. 4a–c for the corresponding legends.

neighboring colony depends greatly on misorientation of the α_2-Ti_3Al lamellae across the colony boundary. That is, when this misorientation is small, the crack easily advances into the neighboring cell. In sharp contrast, when misorientation is large, a higher value of the applied stress intensity factor K_I is required before the crack can continue to advance. This phenomenon gives rise to be characteristic step-wise shape of the fracture resistance curve.

(d) When the advancement of a crack is stalled at a colony boundary, a new crack is nucleated in the neighboring colony and continues to grow with increasing load. This is generally accompanied by formation of a ligament between the main crack and the new crack in the neighboring colony. The ligament bridges the two cracks and it is its failure which entails higher level of the stress intensity factor for crack advancement.

3.2. γ-TiAl + α_2-Ti_3Al material containing stable β-phase precipitates

In this section, the results of the finite element analysis of the mode-I fracture behavior of the γ-TiAl + α_2-Ti_3Al material containing stable β-phase precipitates are presented and discussed.

The normal stress σ_{22}, the hydrostatic pressure $-\sigma_h$, the equivalent plastic strain ε^p and the total lattice rotation angle $\Delta\psi$ contour plots in the inner region of the computational domain at the normalized stress intensity factor $K_I/K_{Ic0}^{\alpha 2} = 4.0$ are shown in Fig. 7a–d, respectively. To enable a quantitative comparison of the results shown in Fig. 7a–d with their counterparts for the γ-TiAl + α_2-Ti_3Al material without β-phase precipitates, Fig. 4a–d, the same levels are assigned to be minimum-value and the maximum-value contour lines. For example, the minimum-value 2.30×10^8 Pa and the

maximum value 1.9×10^9 Pa contour lines are used for the normal stress, σ_{22}.

A careful comparison of the results shown in Fig. 7a–d with the corresponding results shown in Fig. 4a–d suggests that the presence of stable β-phase precipitates has only a minor effect on the deformation fields analyzed. The observations relating the location of the maximum normal stress, $\sigma_{22,}$ and the tensile hydrostatic stress, $\sigma_{h,}$ nonuniformity in the extent of plastic deformation, $\bar{\varepsilon}^{\mathrm{pl}}$, throughout the computational domain and within individual γ-TiAl + α_2-Ti_3Al colonies, etc. previously made in connection within Fig. 4a–d, can still be made. Among the noticeable difference, however, one may note that the presence of more compliant β-phase precipitates reduces the extent of incompatibility in plastic strain between the adjacent colonies. This, in turn, results in somewhat more uniform distribution of the lattice-rotation angle and the plastic strain within the colonies near β-phase precipitates, Fig. 7c–d, in comparison to the ones observed in the β-phase precipitates free material, Fig. 4c–d.

The crack path and the corresponding variation in the crack extension, Δa, with an increase in the applied normalized stress intensity factor, $K_{\mathrm{I}}/K_{\mathrm{Ic0}}^{\alpha 2}$, for γ-TiAl + α_2-Ti_3Al containing stable β-phase precipitates are shown in Fig. 8a–d, and Fig. 6b, respectively. To enable a direct comparison with the corresponding results for the β-phase precipitates free material (Fig. 5a–d), the results shown in Fig. 8a–d are given at the same four values of the applied normalized stress intensity factor $K_{\mathrm{I}}/K_{\mathrm{Ic0}}^{\alpha 2}$ of: 0.77, 1.67, 2.53 and 4.0.

A comparison of the results shown in Fig. 8a–d with their corresponding counterparts for the β-phase precipitates free material shown in Fig. 5a–d, indicate that in the presence of β-phase particles, the crack still extends preferentially along the α_2-Ti_3Al planar surfaces and also along the γ-TiAl + α_2-Ti_3Al colony boundaries which, at times, form ligaments separating delaminated α_2-Ti_3Al planar surfaces and the main crack. In addition, since the resistance for material decohesion is higher along the colony boundaries, the resulting fracture resistance curve acquires the characteristic steplike shape, Fig. 6b. The high-slope portions of the fracture resistance corresponds to the gradual decohesion of the colony-boundary ligaments, while the nearly horizontal portion of the curve corresponds to the process of linking of the main crack and the secondary cracks ahead of it. It should be noted that, at the same level of the applied normalized stress intensity factor, the presence of stable β-phase precipitates gives rise to a lower extent of decohesion along the α_2-Ti_3Al planar surfaces and γ-TiAl + α_2-Ti_3Al colony boundaries, and the extent of extension of the main crack is smaller.

3.3. γ-TiAl + α_2-Ti_3Al material containing matastable β-phase precipitates

In this section, the results of the finite element analysis of the mode-I fracture behavior of the γ-TiAl + α_2-Ti_3Al material containing metastable β-phase precipitates are presented and discussed.

The normal stress $\sigma_{22,}$ the hydrostatic pressure $-\sigma_{h,}$ the equivalent plastic strain ε^{p} and the total lattice rotation angle $\Delta\psi$ contour plots in the inner region of the computational domain at the normalized stress intensity factor $K_{\mathrm{I}}/K_{\mathrm{Ic0}}^{\alpha 2} = 4.0$ are shown in Fig. 9a–d,

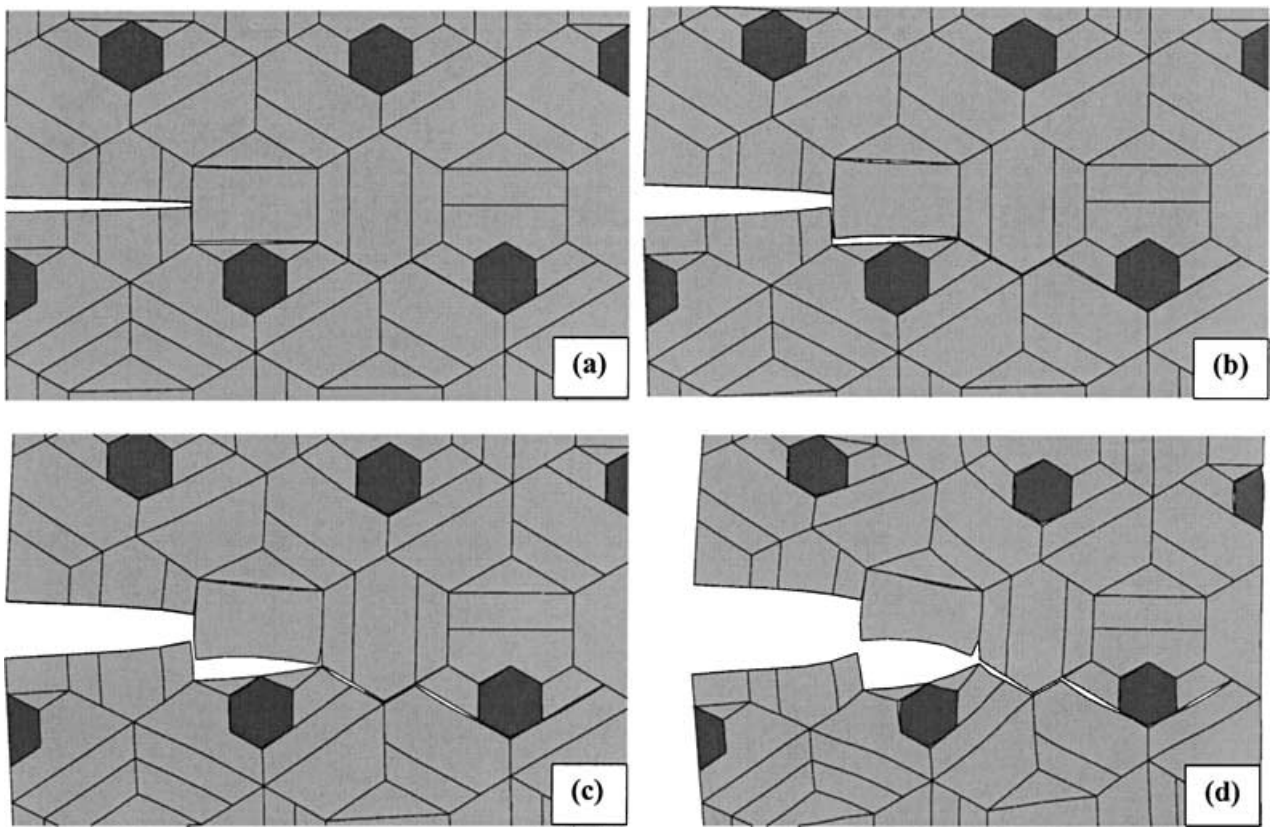

Figure 8 Crack trajectory at four levels of the normalized stress intensity factor $K_{\mathrm{I}}/K_{\mathrm{Ic0}}^{\alpha 2}$ of (a) 0.77; (b) 1.67; (c) 2.53; and (d) 4.00 in γ-TiAl + α_2-Ti_3Al containing stable β-phase precipitates.

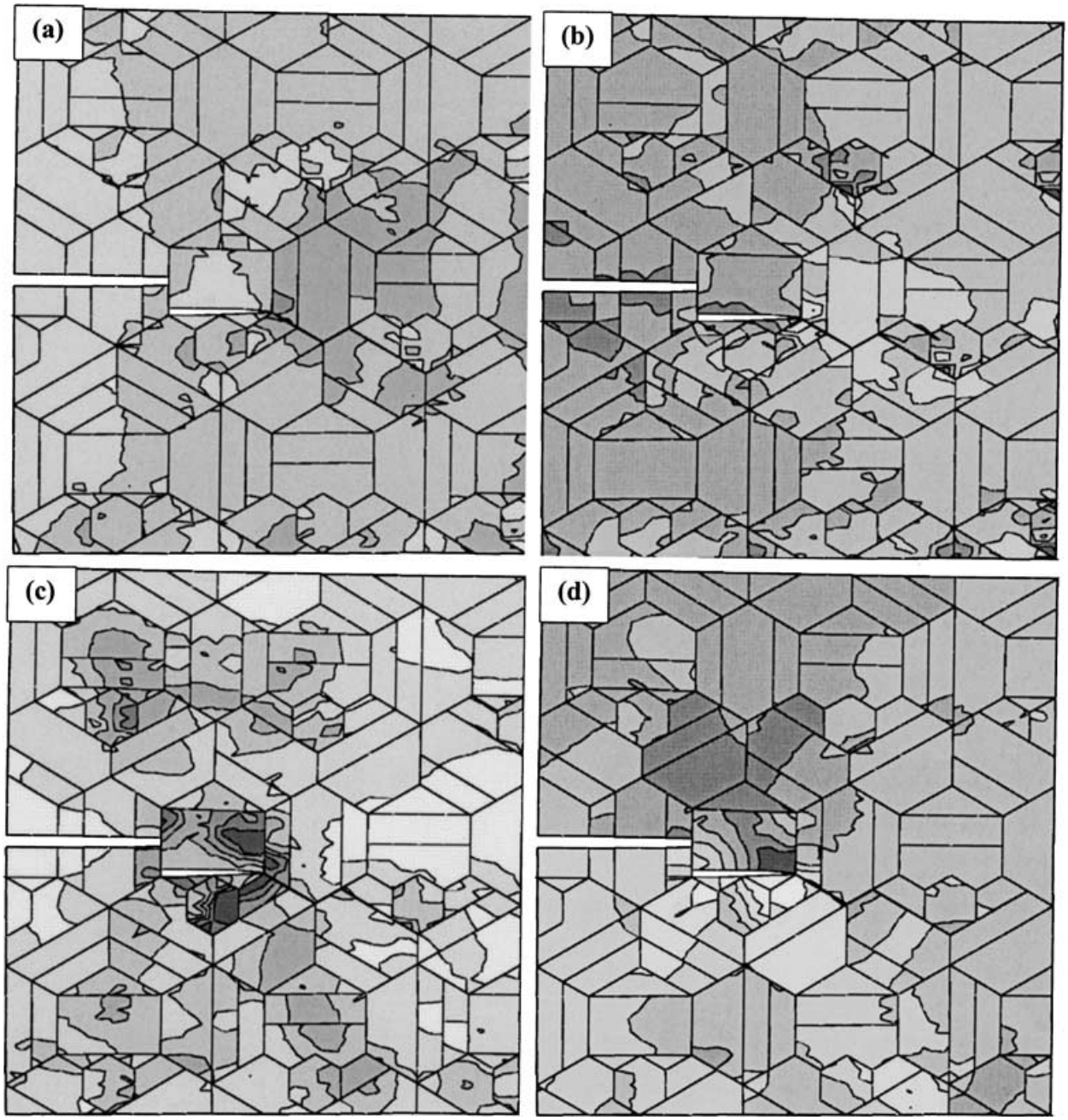

Figure 9 (a) Normal stress, σ_{22}; (b) pressure, $-\sigma_h$; (c) equivalent plastic strain, $\bar{\varepsilon}^{pl}$; and (d) total lattice rotation angle, $\Delta\psi$, contour plots in the γ-TiAl + α_2-Ti_3Al containing metastable β-phase precipitates at the stress intensity factor $K_I/K_{Ic0}^{\alpha 2} = 4.0$. See Fig. 4a–c for the corresponding legends.

respectively. As previously noted in the case of γ-TiAl + α_2-Ti_3Al containing stable β-phase precipitates, the presence of metastable β-phase precipitates has only a minor effect on the deformation fields around the crack tip, Fig. 9a–d. Also, the previously noted effect of precipitates on helping accommodate the plastic strain incompatibilities between adjacent γ-TiAl + α_2-Ti_3Al colonies is still evident in Fig. 9c and d, but is almost identical to that caused by stable β-phase precipitates, Fig. 8c–d. The results shown in Fig. 8a–d appear to suggest that the crack tries to avoid the beta phase particles. A detailed examination of the results showed that this is not a case of elastic interactions due to particle/matrix modulus mismatch but rather a consequence of the fact that the crack chooses to propagate along the surface subject to a maximum normal loading.

The crack path and the corresponding variation in the crack extension with an increase in the applied normalized stress intensity factor, $K_I/K_{Ic0}^{\alpha 2}$, for the γ-TiAl + α_2-Ti_3Al containing metastable β-phase precipitates are shown in Fig. 10a–d and Fig. 6c, respectively. The results shown in these figures indicate that, as in the previous two cases, crack growth takes place preferentially along α_2-Ti_3Al planar surfaces and γ-TiAl + α_2-Ti_3Al colony boundaries. The colony boundaries, act as ligaments separating cracks and provide higher resistance to crack extension giving rise to steep rises in the fracture resistance curve. These findings are in a very good agreement with the experimental observations of Chan and Shih [29] in a two-phase lamellar TiAl + Ti_3Al sheet alloy with an average colony size of approximately 15 m.

A careful comparison of Fig. 10a–d and Fig. 6c with their counterparts for γ-TiAl + α_2-Ti_3Al containing stable β-phase precipitates, Fig. 8a–d and Fig. 6b, indicates that metastable precipitates are more effective

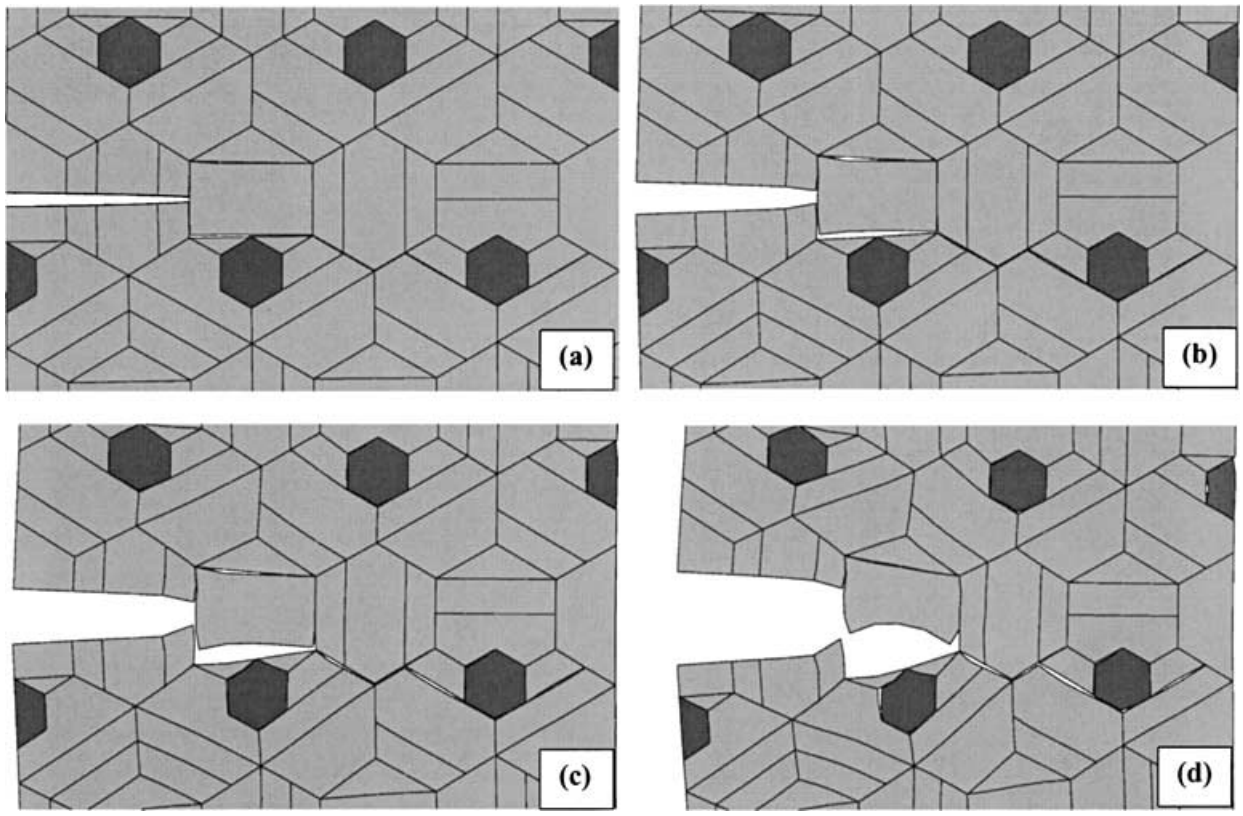

Figure 10 Crack trajectory at four levels of the normalized stress intensity factor $K_I/K_{Ic0}^{\alpha 2}$ of (a) 0.77; (b) 1.67; (c) 2.53; and (d) 4.00 in γ-TiAl + α_2-Ti_3Al containing metastable β-phase precipitates.

in hindering crack growth. This finding is consistent with the experimental observation of Grujicic and Dang [2] and can be ascribed to be effect of martensite transformation in the metastable β-phase which, due to an attendant positive value change, acts as a crack-tip toughening mechanism.

4. Conclusions

Based on the results obtained in the present study the following main conclusions can be drawn:

- In agreement with the experimental observations of Chan *et al*. [27], the predominant fracture mechanism in γ-TiAl + α_2-Ti_3Al fully-lamellar material is decohesion alogn the planes parallel with the α_2-Ti_3Al lamellae which gives rise to formation of secondary cracks ahead of the tip of the main crack. At higher applied loads, the ligaments separating the main crack and the secondary cracks fail causing an abrupt crack extension. Ligaments failure typically takes place along the γ-TiAl + α_2-Ti_3Al colony boundaries.
- Failure of the ligaments separating cracks entails a higher applied load. However, once a ligament fails the main crack abruptly extends over the entire neighboring colony (and frequently over more than one colony) at an essentially constant level of the applied stress intensity factor. This fracture mode gives rise to a characteristic step-wise shape of the fracture resistance curve.
- The presence of stable and metastable β-phase precipitates has a minor effect on the deformation fields surrounding the advancing crack tip. However, the presence of β-phase precipitates which can undergo plastic deformation (and a strain-producing phase transformation) enhances damage tolerance of the γ-TiAl + α_2-Ti_3Al fully-lammellar material. In other words, the extent of growth of the pre-existing crack is smaller in the material containing β-phase precipitates.

Metastable β-phase precipitates appear to have a somewhat larger beneficial effect on fracture resistance of the γ-TiAl + α_2-Ti_3Al fully-lamellar material than stable β-phase precipitates. This finding is an indication of the transformation toughening effect arising from a volume-enhancing martensitic transformation in metastable β-phase precipitates.

Acknowledgements

The material presented here is based on work supported by the National Science Foundation, Grant Numbers DMR-9906268 and CMS-9531930 and by the U.S. Army Grant Number DAAH04-96-1-0197. The authors are indebted to Drs. Bruce A. MacDonald and Daniel C. Davis of NSF and Dr. David M. Stepp of ARO for the continuing interest in the present work. The authors also acknowledge the support of the Office of High Performance Computing Facilities at Clemson University.

References

1. K. S. CHAN and Y.-W. KIM, *Metallurgical Transactions* A **23** (1992) 1663.
2. M. GRUJICIC and P. DANG, *Materials Science and Engineering* A **224** (1997) 1987.

3. K. S. CHAN and Y.-W. KIM, *Metallurgical Transactions* A **25** (1994) 1217.
4. *Idem.*, *Acta Metallurgica et Material* **43** (1995) 439.
5. S. MITAO, T. ISAWA and S. TSUYAMA, *Scripta Metallurgica et Material* **26** (1992) 1405.
6. K. S. CHAN, *Metallurgical Transactions* A **24** (1993) 569.
7. K. S. CHAN, J. ONSTOTT and K. S. KUMAR, *ibid.* A **31** (2000) 71.
8. L. HEATHERLY, E. P. GEORGE, C. T. LIU and M. YAMAGUCHI, *Intermetallics* **5** (1997) 281.
9. S. YOKOSHIMA and M. YAMAGUCHI, *Acta Material* **44** (1996) 873.
10. B. K. KAD, M. DAO and R. J. ASARO, *Materials Science and Engineering* A **192/193** (1995) 97.
11. *Idem.*, *Phil. Mag*. A **71** (1995) 567.
12. M. GRUJICIC and Y. ZHANG, *Materials Science and Engineering* A **265** (1999) 285.
13. *Idem.*, *J. Mater. Sci*. **34** (1999) 1419.
14. M. GRUJICIC and S. BATCHU, *ibid.*, submitted.
15. M. GRUJICIC, G. CAO and S. BATCHU, *Materials Science and Engineering*, submitted.
16. M. GRUJICIC and S. G. LAI, *J. Mater. Sci*. **33** (1998) 4401.
17. *Idem.*, *ibid*. **33** (1998) 4388.
18. J. J. M. ARATA and A. NEEDLEMAN, *International Journal of Fracture* **94** (1998) 383.
19. J. J. M. ARATA, A. NEEDLEMAN, K. S. KUMAR and W. A. CURTIN, *ibid.*, in press.
20. *Idem.*, to be published.
21. A. NEEDLEMAN, *Journal of Applied Mechanics* **54** (1987) 525.
22. X. P. XU and A. NEEDLEMAN, *Journal of the Mechanics and Physics of Solids* **42** (1994) 1397.
23. P. WANG, N. BHATE, K. S. CHAN and K. S. KUMAR, in High Temperature Ordered Intermetallic Alloys IX, Proceedings of Materials Research Society Symposium, Vol. 646, edited by J. H. Schneibel, K. J. Hemkar, R. D. Noebe, S. Hanada and G. Sauthoff (MRS, Pittsburgh, PA, 2001).
24. K. S. KUMAR, P. WANG, K. CHAN, J. ARATA, N. BHATE, J. ONSTOTT, W. CURTIN and A. NEEDLEMAN, in "Structural Intermetallics 2001," edited by K. J. Hemker, D. M. Dimiduk, H. Clemens, R. Darolia, H. Inui, J. M. Larsen, V. K. Sikka, M. Thomas and J. D. Whittenberger (TMS, Warrendale, 2001) p. 249.
25. T. SIGMUND and A. NEEDLEMAN, *International Journal of Solids and Structure* **34** (1997) 769.
26. Abaqus User's Manual, Version 5.8, Hibbitt, Karlsson and Sorensen, Inc., Providence, RI., 1998.
27. M. GRUJICIC and N. SANKARAN, *Inter. Journal of Fracture* **83** (1997) 337.
28. W. G. BURGERS, *Physica* **1** (1934) 561.
29. K. S. CHAN and D. S. SHIH, *Metallurgical and Material Transactions* A **28A** (1997) 79.

Received 4 June 2001
and accepted 27 March 2002